Photocatalytic degradation of trichloroethylene in a continuous annular reactor using Cu-doped TiO₂ catalysts by sol–gel synthesis

Daniela Xulú Martínez Vargas [a], Javier Rivera De la Rosa [a,b,*], Carlos J. Lucio-Ortiz [a], Aracely Hernández-Ramirez [a], Gerardo A. Flores-Escamilla [a], Carlos D. Garcia [c]

[a] Universidad Autónoma de Nuevo León, UANL, Facultad de Ciencias Químicas Ave. Universidad S/N, Cd. Universitaria, San Nicolás de los Garza, N.L. C.P. 64450, Mexico
[b] Universidad Autónoma de Nuevo León, UANL, Centro de Innovación, Investigación y Desarrollo en Ingeniería y Tecnología (CIIDIT), Km 10 de la Nueva Carretera al Aeropuerto Internacional de Monterrey, PIIT Monterrey, Apodaca, Nuevo León C.P. 66600, Mexico
[c] Department of Chemistry, The University of Texas at San Antonio, One UTSA Circle, San Antonio, TX 78249, USA

ARTICLE INFO

ABSTRACT

In this work, we present the capability to address sustainability at the molecular level for Green Chemistry. Cu-doped (up 0.5 wt%) TiO₂ catalysts were prepared by sol–gel, calcined at 500 °C supported on quartz tubes, and placed into a continuous annular reactor to degrade a trichloroethylene (TCE)/air mix in moist stream. To understand how the Cu content affects the photocatalytic activity of the modified catalyst, the deposited and calcined washcoat on the quartz materials was characterized. The powder catalysts were also characterized to correlate their properties with their behavior on the quartz tubes and in the tests using a continuous photocatalytic reactor. A Langmuir–Hinshelwood kinetic model that considers two active sites (one for active TCE molecules and the other for active H₂O molecules) was fitted to the reaction data. The catalyst doped with 0.2 wt% Cu showed the best performance in the degradation tests. Notably, this catalyst differed from the other three with 0, 0.05 and 0.5 wt% Cu because it had the lowest E_g and uniform porosity. The activation energy and adsorption thermodynamic property constants demonstrated that 0.2 wt% Cu content favored the mobility of both molecules, while 0.5 wt% Cu strongly obstructed the active sites through bonding with water.

© 2015 Elsevier B.V. All rights reserved.

1. Introduction

Volatile organic compounds (VOCs) are recognized as dangerous to the environment and human health. Common VOCs include alcohols, ethers, ketones and chlorinated compounds [1]. Among the chlorinated VOCs, trichloroethylene (TCE) is widely used in industry as a solvent and a cleaning and degreasing agent [2,3]. Because TCE is considered one of the most toxic and carcinogenic VOCs [3,4], its elimination from or decomposition in the environment has become an important issue for investigation. Viable processes for reducing VOCs (including TCE), such as thermal combustion, catalytic combustion, adsorption, and biofiltration, have been developed [1,5,6]. Nevertheless, these processes are not entirely satisfactory due to their low efficiency or high energy consumption [1,5]. Therefore, more cost-effective mitigation techniques are required to meet the increasingly stringent emissions regulations worldwide, contributing to the development of Green Chemistry. New processes must be recognized for their ability to address sustainability at the molecular level [7].

One of the most investigated processes is the catalytic oxidation of TCE under heterogeneous conditions [5,8–13]. Metal-supported catalysts based on noble metals (e.g., Pt, Ru, Pd) [9,10,13] or other transition metals (e.g., Mn, Ni, Co) [11,12] have been demonstrated to be effective in the degradation of TCE under moderate conditions. However, in most cases, the catalysts are reported to be deactivated during the TCE catalytic oxidation, mainly due to the formation of chlorinated by-products, volatilization of the catalysts, coke deposition and thermal degradation [8].

Heterogeneous photocatalysis can be carried out at lower temperatures (<100 °C), and the production of Cl₂ can be mitigated by performing the reaction under humid conditions, which favor the Deacon reaction [14] to form HCl and •OH on the photocatalyst surface (oxidative agents). Furthermore, in gaseous heterogeneous photocatalytic processes, the formation of hazardous products such
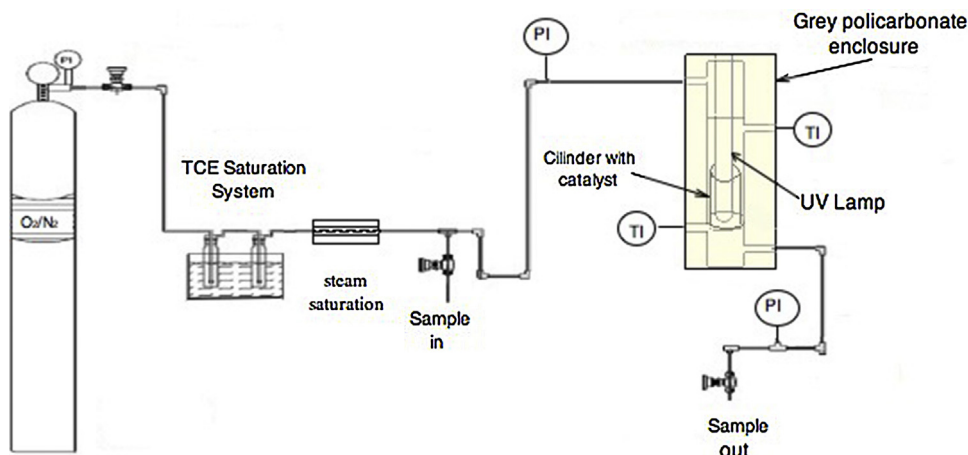
Fig. 1. Experimental setup for kinetic tests of trichloroethylene in moist air in a continuous annular reactor.
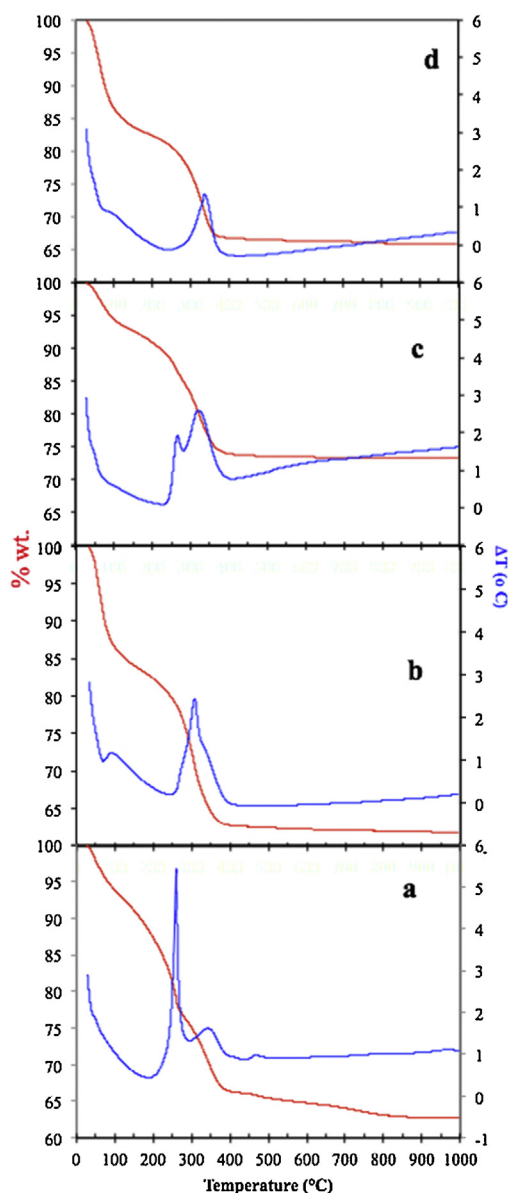

Fig. 2. TGA and DTA of TiO$_2$ (a) and doped with 0.05 (b), 0.2 (c) and 0.5 % wt. (d) of Cu. (For interpretation of the references to color in the text, the reader is referred to the web version of this article.)

as phosgene and chloroform can be reduced by using modified photocatalysts [15].

TiO$_2$ is the most common semiconductor photocatalyst used in gaseous heterogeneous TCE degradation. TiO$_2$ has the appropriate properties (i.e., chemical stability, non toxic and suitably positioned valence and conduction band edges) to degrade VOCs, assisted by UV radiation [16,17]. Since Dibble and Raupp [18] reported the first degradation of TCE in the gas phase using TiO$_2$ as a photocatalyst, many studies have been performed to improve the catalytic activity of TiO$_2$ and to understand the reaction mechanism [1–4,6,19,20].

One of the studied alternatives is the doping of TiO$_2$ with other metals. The addition of metallic species to TiO$_2$ has been reported to enhance the photocatalytic activity by changing the properties of the semiconductor surface. The metal may increase the production of particular species, affecting the rate of the photocatalytic reaction [21]. This doping promotes the separation of holes and electrons to prevent recombination; alternatively, some species may act as an electron trap [22]. However, doping with metals do not always have a positive effect on the activity of photocatalysts and can even decrease their activity [16,23]. Therefore, the structural changes to TiO$_2$ after its modification with metals must be evaluated and carefully considered to avoid the formation of hazardous by-products.

Although some studies have successfully used Cu as a dopant to improve the photocatalytic activity of TiO$_2$ in the degradation of some organic compounds and dyes (e.g., phenol [24], o-xylene [25], 2-propanol [26] and methylene blue [27]), only a few investigators have reported using Cu-doped TiO$_2$ photocatalysts in the degradation of TCE [6,15,27].

Tanimura et al. [15] proposed incorporating Cr, Fe, Ni, Cu, Pt, and Ca(OH)$_2$ (above 5 wt%) by mixing with TiO$_2$ that had been previously synthesized by the sol–gel method. They reported that modification with Cu and Ca(OH)$_2$ decreased the formation of chlorinated by-products (phosgene and chloroform). However a significant increase in the activity during the degradation of TCE using doped TiO$_2$ with Cu or Ca(OH)$_2$ was not observed, even when a high metal content was used in the photocatalysts (approximately 50%). Furthermore, the aggregation of the dopants could lead to the deactivation of the photocatalysts. Recently, Nishikiori et al. [27] carried out the photocatalysis of TCE in presence of Cu-doped TiO$_2$ samples synthesized by sol–gel. They found that the dopant was homogeneously dispersed on the TiO$_2$, leading to a useful interaction between the Cu^{2+} and Ti^{4+} centers. Their results show that the Ti–O–Cu interaction promotes photocatalytic activity and electron trapping, as well as the activation of the photocatalyst under visible light radiation.

The investigations discussed above show the degradation capability of Cu-doped TiO$_2$ systems. Therefore, searching for better reaction conditions and discovering the structural properties of photocatalysts and kinetic parameters during the photodegradation of TCE in the gas phase using Cu-doped TiO$_2$ as the photocatalyst continues.

Among the methods of TiO$_2$ synthesis, the sol–gel method can provide important microstructural characteristics such as surface morphology and roughness [2]. The sol–gel technique is an attractive method for preparing doped catalysts because the constituents are mixed at the atomic scale, generating a uniform distribution of dopants on the support.

In this study, Cu-doped (up 0.5 wt%) TiO$_2$ catalysts were prepared by sol–gel, calcined at 500 °C supported on quartz tubes, and placed into a continuous annular reactor to degrade TCE. To understand how the Cu content affects the photocatalytic activity of the modified catalyst, the deposited and calcined washcoat on the quartz materials was characterized. The characterization of the solid samples was accomplished by Differential Thermal Analysis and Thermogravimetric Analysis (DTA and TGA), X-ray Diffraction (XRD), Ultraviolet-Visible spectroscopy (UV–vis), Fourier transform infrared spectroscopy (FTIR), Inductively Coupled Plasma (ICP), N$_2$ adsorption and X-ray photoelectron spectroscopy (XPS). The powder catalysts were also characterized to correlate some of their properties with their behavior on the quartz tubes and in the continuous photocatalytic reactor tests. A Langmuir–Hinshelwood kinetic model (dependency of the photocatalytic reaction rate on the concentration of the organic substrate has been generally well described for this kind of model [28,29]) was fitted to the reaction data from a continuous annular reactor at three temperatures, and the kinetic and adsorption parameters were analyzed. This work contributes to Green Chemistry by providing information about sustainability at the molecular level, and it contributes to the understanding of the kinetic mechanism and action of Cu when added to a TiO$_2$ photocatalyst for gaseous TCE degradation.

2. Experimental

2.1. Sol formulation

The molar ratio of the precursors was formulated to obtain a compact film without cracks on silica substrates. The molar ratio of titanium butoxide to H$_2$O was 1 to 1.76 and that of titanium butoxide and to *n*-butanol was 1 to 32.3; all reagents were provided by Sigma–Aldrich (Milwaukee, WI, USA). The titanium butoxide and 72.92 v% *n*-butanol used in the synthesis were mixed continuously for 1 h. The pH was adjusted to 4 by adding acetic acid dropwise, and the mixture was stirred for an additional 30 min. Hydrolysis was subsequently initiated by adding the remaining *n*-butanol, suspended in H$_2$O, dropwise. An ultrasound bath was used to obtain a homogenous sol. The same procedure was followed to obtain the Cu-doped catalyst, with the following difference: the copper precursor (copper II acetate, dissolved in 1 mL of water required for hydrolysis) was added dropwise after adding half of the *n*-butanol and water suspension. The doped TiO$_2$ catalysts were prepared with different weight percentages of Cu II: 0.05, 0.2 and 0.5 wt% (TiO$_2$-0.05, TiO$_2$-0.2 and TiO$_2$-0.5, respectively), equivalent to 0.062, 0.251 and 0.627 mol% (atom%).

2.2. Dip-coating deposition

After 24 h, the synthesized sol was used to prepare the supported catalyst by dip-coating. A mechanical dispositive was used to coat pieces of quartz; the velocity of immersion was 100 cm/min. Next, the catalyst-coated quartz pieces were dried for 15 min at

50 °C and, finally, annealed at 500 °C for 1 h at a heating rate of 10 °C /min. This procedure was repeated until approximately 5 mg of catalyst was deposited on quartz plates and quartz cylinders.

Quartz plates (5 × 10 cm) were used for spectroscopic ellipsometry tests, and quartz cylinders (2.9 cm internal diameter and 4 cm high) were used for continuous reactor experiments.

2.3. Catalyst powders

The synthesized sols were maintained in sealed beakers at room temperature until gel formation (45 days). The formation of xerogels was achieved by drying the gels at 80 °C. The xerogels were calcined at 500 °C for 6 h at a heating rate of 10 °C / min.

2.4. Characterization techniques

Thermal analysis of the xerogels was carried out in air by heating to 1000 °C at a heating rate of 5 °C/min using a TA Instruments SDT-2960 thermal analyzer. Analysis of the crystalline phase of the powders calcined at 500 °C was performed by X-ray diffraction (XRD) using a Siemens D5000 diffractometer (Siemens Inc., Berlin, Germany), with Ni-filtered Cu Kα radiation in the 2θ range (5–110°) at a scan rate of 0.020°/min.

The FTIR spectra of the samples, in the form of KBr mixed disks, were measured using a Nicolet^{TM} 6700 spectrometer (Thermo Scientific, Waltham, MA, USA). The management software for sample analysis was OMNIC^{TM} (Thermo Scientific) in transmittance mode. The spectra were acquired with 32 scans using a resolution of 4 cm^{-1}.

UV–vis diffuse reflectance spectra of calcined powders were recorded on a Nicolet Evolution 300 PC UV–vis spectrophotometer (Thermo Scientific, Waltham, MA, USA). N$_2$ sorption isotherms at 77 K were recorded using an Autosorb-1 volumetric instrument (Quantachrome Co., Boynton Beach, FL, USA). Prior to adsorption runs, all samples were degassed overnight at 200 °C. Ultra high purity (UHP) grade N$_2$ and He gases were required for the adsorption instrument. Scanning electron micrographs (SEM) were obtained on an FEI Nova Nano SEM200 (FEI, Hillsboro, OR, USA) operated at 30 kV and 50 mA at a 9-mm working distance.

A variable-angle spectroscopic ellipsometer (VASE, JA Woollam Co., Lincoln, NE) was used to measure film thicknesses. The spectral range from λ = 2500 to 8000 Å was covered using a wavelength interval of 20 nm and a beam with a spot size of 3 mm at angles of incidence ϕ = 65° and ϕ = 75°.

Quantitative analysis of the copper content was performed by inductively coupled plasma (ICP) using a dual Thermo Fisher Scientific iCAP 6500 (Thermo Scientific, Waltham, MA, USA).

Surface analysis were made with a X-ray photoelectron spectrometer K-Alpha de Thermo Scientific, with X-ray spot of 400 nm, using the flood gun for charge compensation. Mesurements were performed after ion beam etch with argon ion gun (2 keV during 20 s with 20–40 nm estimated thickness.

2.5. Photocatalytic tests in a continuous annular reactor

The photocatalytic tests were performed using the catalytic continuous annular reactor depicted in Fig. 1. The inlet mixture of TCE in air was prepared by bubbling air into liquid TCE in a temperature-controlled saturation system to vary the inlet concentration of TCE for kinetic tests. Next, the stream was moistened by saturating the gases at 25 °C by passing them through a membrane tube immersed in a closed vapor water-containing thermostatic bath. A flow of 200 mL/min of TCE at different concentrations (in air at STP) was passed through the quartz cylinder with the catalyst deposited on the interior wall. The annular space with catalyst present had external and internal diameters of 2.7 cm and 1.5 cm, respectively and

Table 1
Textural properties of calcined powder TiO_2 samples.

Sample	Cu wt%[a]	Mean size of crystallite (nm)	S_{BET}[b] (m^2/g)	Pore volume[c] (cm^3/g)	Pore size[c] (nm)	Eg (eV)
TiO_2	0.0	33	40.80	0.06	0.45-5.47	3.04
TiO_2-0.05	0.054	33	55.17	0.08	0.41-5.49	3.06
TiO_2-0.2	0.180	29	60.27	0.12	2.90-8.74	2.95
TiO_2-0.5	0.457	35	35.64	0.06	1.58-5.74	2.74

[a] Using Inductively coupled plasma (ICP) technique.
[b] Brunauer–Emmett–Teller method.
[c] Barrett–Joyner–Halenda method.

was 4 cm in height. A Spectroline 36-360 quartz pencil lamp (Radiatronics Ndt-Inc., Shawnee Mission, KS, USA) was used at $\lambda = 360$ nm, at $1000 \mu W/cm^2$. The space velocity (SV), calculated by dividing the volumetric flow by the annular reactor volume, was $682 h^{-1}$, and the weight hourly space velocity (WHSV), which is defined as the weight of feed flowing per unit weight of the catalyst per hour, was $2829 h^{-1}$.

The concentration of chlorinated hydrocarbons (TCE, tetrachloroethene, 1,1,1-trichloroethane) was determined using a model HP5890 II gas chromatograph (Wilmington, DE, USA) equipped with a flame ionization detector (FID) using a DB-624 capillary column with ID 0.32 mm (Agilent, Santa Clara, CA, USA). The concentrations of CO_2 and CO products were measured online by an IR spectrometer California Analytical, model 20 (Orange, CA, USA). To determine the HCl and Cl_2 concentrations, the gas flow containing the product was passed through two containers with 100 ml of NaOH (0.0125 N), and the chlorine concentration was measured by the N,N-diethyl-p-phenylenediamine (DPD) method using a DR-890HACH instrument (method 8167). The concentration of hydrochloric acid was quantified by the Mohr method [10].

3. Results and discussion

3.1. Thermal analysis of powders

Table 1 reports the copper content of the different prepared catalysts in powder form. The copper composition determined by ICP analysis was very close to the expected value determined during the synthesis methodology.

Fig. 2 shows the differential thermal analysis (DTA) and thermogravimetric analysis (TGA) results on the same plot for xerogel samples dried at 80 °C. For TiO_2 samples, TGA (red line Fig. 2a) exhibits an initial weight loss (21.53 %) from room temperature to 262 °C, which is attributed to the loss of physically absorbed water, butanol and acetic acid from the xerogel. A second weight loss of 32.9 % is observed from 262 °C to 374 °C, associated with the combustion of organics and loss of alkoxy groups.

A final weight loss, observed from 374 to 1000 °C, can be attributed to strong alkoxy groups in this sample, which are generally completely lost below 500 °C. The DTA curve of the same sample (blue line, Fig. 2a) shows a broad endothermic peak at 200 °C, which confirms water desorption. A sharp peak at 260 °C corresponds to combustion of organic compounds; the exothermic peak at 334 °C can be related to the combustion of the remaining alkoxy groups, which is a result of incomplete hydrolysis/condensation reactions[30]. A small peak observed at 460 °C could be attributed to the reorganization of the inorganic matrix after removal of the organic components from the amorphous to the anatase phase during transformation. Fig. 2b shows TGA data for TiO_2-0.05, which exhibits three steps of weight loss: the first and second at 98 and 250 °C represent 14 and 20 % weight loss, respectively, and the third at 372 °C represents 37 % weight loss. These events are attributed to the same principles as the TiO_2 sample. In the DTA data for sample TiO_2-0.05, the most significant difference

is the overlap of the two exothermic peaks: the maximum occurs at 309 °C, a shoulder occurs at 340 °C and the peak ends at 400 °C; the exothermic peak corresponding to the anatase phase formation was not observed at 460 °C due to the presence of copper, which causes the transformation to occur at a lower temperature. For sample TiO_2-0.2, the TGA curve also exhibits three weight loss steps at nearly the same temperatures as the other samples, but this sample lost the smallest amount of weight compared to the other samples, losing only 26.74 % when heated to 1000 °C. This difference indicates that from the preparation of the xerogel to a temperature of 80 °C, this sample lost more physically adsorbed water than the others. In the DTA data for the same sample, the maxima of the peaks, which correspond to the combustion of organic desorbed compounds, were shifted to lower temperatures compared to the other samples, with maxima at 262 and 322 °C. This result demonstrates that 0.2 wt% Cu during synthesis favors the desorption and combustion of alkoxy groups at lower temperatures due to the differences in the morphological characteristics that were obtained for the final calcined sample (presented in SEM images of powder section). For sample TiO_2-0.5 (0.5 wt% Cu), the TGA curve shows behavior similar to the TiO_2 and the TiO_2-0.05 samples, with a total loss of 36.2 % after heating to 1000 °C. The DTA curve of TiO_2-0.5 shows a defined exothermic peak with a maximum at 334 °C; the desorption and combustion of alkoxy groups occur in one event at 0.5 % Cu. The exothermic peaks at the 250-400 °C range are related to the oxidation and burning of the released organic impurities. The exothermic peak at lower temperature may be attributed to the decomposition and oxidation of acetate chelate (cleavage of Ti—O bond in $(TiO_2)_n$—O—CO—CH_3) and at higher temperature is attributed to the rupture and oxidation of alkoxy (cleavage of Ti–O bond in $(TiO_2)_n$—O—C_4H_9) [31,32]. The reason of a wider peak and overlapping with copper doped TiO_2 samples is due to more amorphous TiO_2 crystallizes and releases energy in this temperature range and the dopant used shift the transformation of amorphous TiO_2 to anatase to lower temperatures. The differences of temperature and intensity of the exothermic peaks could be associated with the differences in the textural properties as specific surface area, pore volume, pore diameter and also with the complex species that could be formed with copper (in doped TiO_2 samples). Both TiO_2-0.2 and TiO_2-0.5 samples present a positive slope in their DTA curves from ~390 to 1000 °C (region where the oxide species is formed), which is related to a change in thermal diffusivity $\alpha = k/(\rho C_p)$, where k is the thermal conductivity, ρ is the density, and C_p is the specific heat capacity of the solid material; Cu content above 0.2 wt% changes the properties of the calcined photocatalysts with respect to pure TiO_2.

3.2. FTIR analysis of powders

Fig. 3 shows the FTIR analysis of the fresh (xerogels at 80 °C) and calcined (500 °C) samples. All fresh samples show a broad band from 2400 to 3700 cm^{-1}, which corresponds to the stretching vibrations of hydroxyl groups from water molecules and n-butanol adsorbed to the xerogel powders and from the titanium hydroxide formed. The absorption band at 1640 cm^{-1} is characteristic of the
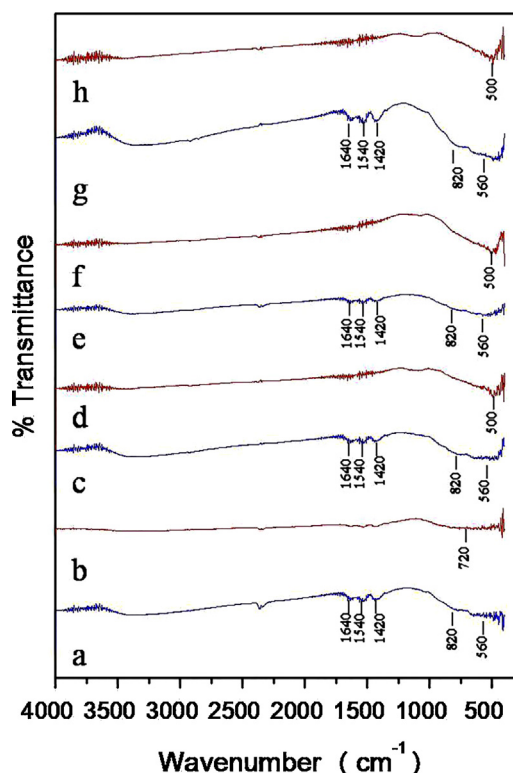
Fig. 3. FTIR of TiO_2 (a), TiO_2-0.05 (c), TiO_2-0.2 (e), TiO_2-0.5 (g) fresh samples and their calcined samples; b, d, f and h, respectively.

Fig. 4. XRD patterns of TiO_2 (a) TiO_2-0.05 (b), TiO_2-0.2 (c), and TiO_2-0.5 (d) powder samples calcined at 500 °C.

bending mode of the H—O bond due to the deformation vibration mode of chemisorbed water. The intensity of the hydroxyl band in TiO_2 fresh samples is notorious (Fig. 3a,c,e,g). This hydroxyl band is related to the large numbers of hydroxyl groups observed in TGA; both bands decrease significantly until almost disappears in the calcined samples. The small band at 2350 cm^{-1} is assigned to CO_2 in the atmosphere [33]. The bands at 1540 and 1420 cm^{-1} observed in the xerogels powders belong to asymmetric ν_{as} and symmetric ν_s of carboxyl (COO) group from the acetic acid adsorbed [34]. The bands attributed to tetrahedral Ti-O stretching ($\sim$820 cm^{-1}) and octahedral Ti—O stretching ($\sim$560 cm^{-1}) are present in xerogel samples, while the calcined samples showed the intensity of the tetrahedral Ti—O band decreased and that of the octahedral Ti-O band increased [35,36] The characteristic stretching vibrations of the inorganic Ti—O—Ti network [37,38] are present in the calcined TiO_2 samples between 400 and 800 cm^{-1} are attributed to O-Ti-O from crystalline titania in the anatase form [35]. This band is broader in copper doped TiO_2 samples, one explanation could be the contribution due the stretching vibrations of Cu^I-O and Cu^{II}-O reported in other studies at 525 cm^{-1} [37] from CuO samples [39] .The changes of IR spectra on TiO_2 doped indicated that the addition of copper oxide affected the titanium surface oxide species and also because Fourier transform infrared (FT-IR) spectrum was sensitive to variations in particle size, shape and morphology [40]. The incorporation of copper into the doped calcined samples promoted a shift to lower wavenumbers for the Ti—O—Ti antisymmetric stretch of the oxo-bridged titanium (IV) compounds on the surfaces. Previous research reported that bands below 1000 cm^{-1} are related to the stretching vibration mode M—O due the formation of metal oxides [37], due to the small amount of copper is expected the band correspond majority to Ti-O and a small contribution of Cu—O. However, the behavior showed in the Fig. 3 for copper doped samples could be due the Cu—O stretching vibrations despite the low amounts of dopant.
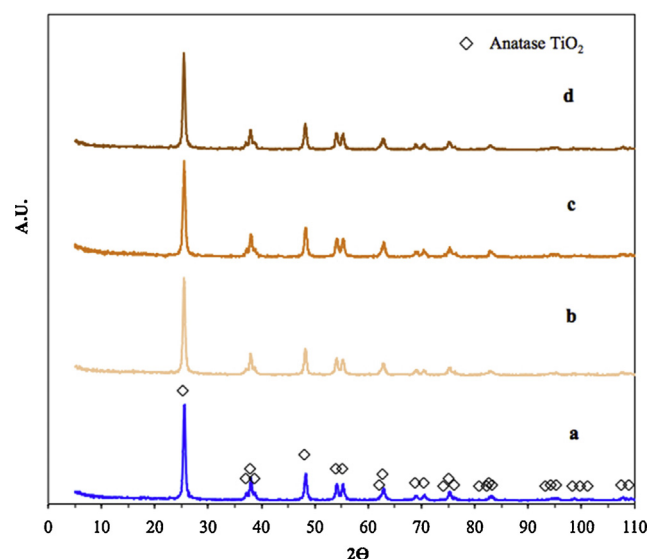
3.3. XRD patterns

Fig. 4 shows the XRD results for the samples calcined at 500 °C. The anatase TiO_2 crystalline phase was identified by planes that are characteristic of TiO_2 samples, according to the Joint Committee on Powder Diffraction Standards (JCPDS) 21-12-72 powder diffraction file. The other samples presented also display only this crystalline phase. Copper oxide species were not identified due to the low weight percentages ($\leq$5 wt%). The mean crystallite size was calculated from the line broadening of the XRD peak of anatase TiO_2 (1 0 1) ($2\theta = 25.28$ in Fig. 4) using the Scherrer equation [41]. Table 1 shows the mean crystallite sizes calculated with the Scherrer equation for all samples.

The crystallite sizes for TiO_2 and TiO_2-0.05 had the same mean. However, incorporating 0.2 wt% copper caused a decrease in this calculated characteristic (from 33 to 29 nm), and increasing to 0.5 wt% copper produced samples with larger crystallites (mean size of 35 nm). This finding shows that copper affects crystallite growth during synthesis, proving that copper functioned as a doping agent.

3.4. Textural analysis from N_2 isotherms

Fig. 5 presents the N_2 adsorption-desorption isotherms at 77 K for powder catalyst samples. In the adsorption-desorption isotherms, red and blue open symbols indicate adsorption and desorption values, respectively. IUPAC classifies the shapes of adsorption isotherms as type IV for the four samples [27], with a hysteresis loop that is associated with capillary condensation within the mesoporous regions. The hysteresis loop for all samples is type H3, which is usually indicative of aggregates of platelet particles or adsorbents containing slit pores. The initial part of the isotherm (until $p/p° \approx 0.42$) can be attributed to monolayer/multilayer adsorption because it follows the same path of desorption, which demonstrates weak adsorbate/adsorbent interactions. The hysteresis loops of all samples begin at $p/p^0 = 0.42$ and end at $p/p^0 = 0.85$; the hysteresis loops exhibit limited adsorption. This phenomenon is related to the presence of particles that are not rigidly joined together. The TiO_2-0.2 sample (Fig. 5c) reached the highest value of adsorption at the saturation point ($p/p^0 = 1$). This phenomenon is related to the greater surface area of this sample, as shown in Table 1, and the better interconnection of pores
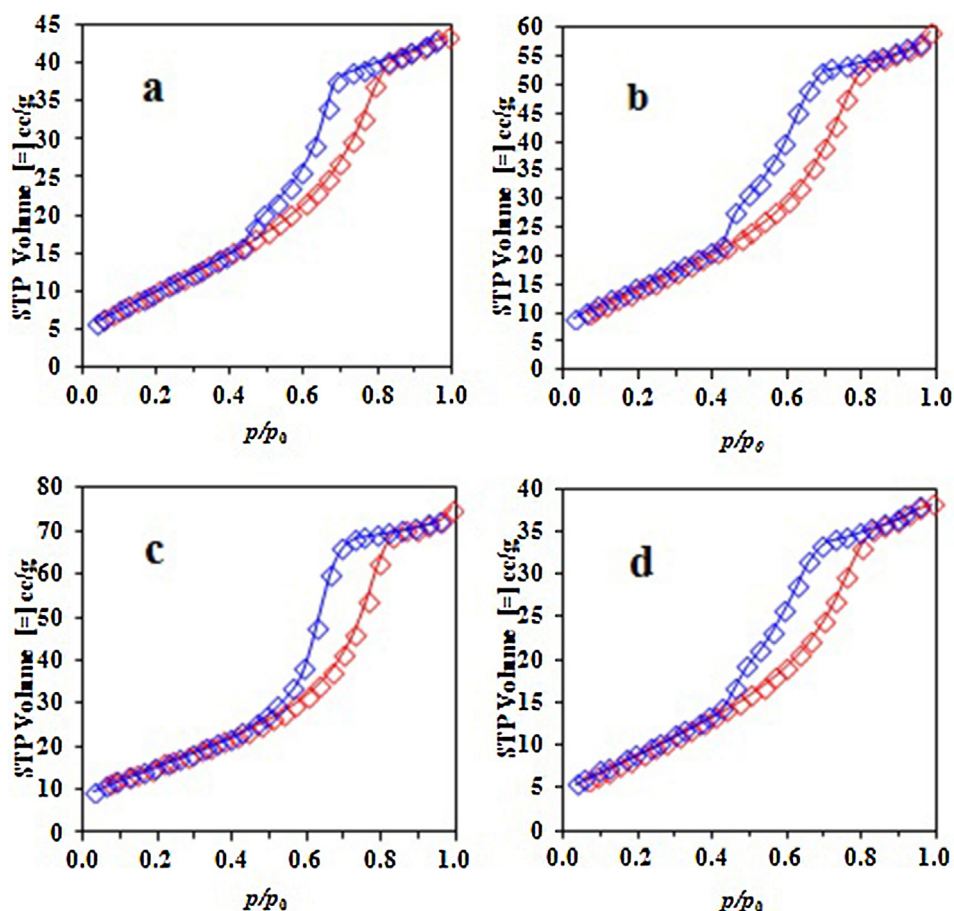
Fig. 5. N_2 physisorption isotherms for samples TiO_2 (a), TiO_2-0.05 (b), TiO_2-0.2 (c), and TiO_2-0.5 (d).

within the particles, which can favor percolation phenomena in continuous photocatalytic tests. The incorporation of 0.5 wt% copper decreased the capacity for adsorption (40 cc/g at $p/p^0 = 1$) in TiO_2-0.5 (Fig. 5d), which can be attributed to pores blocked by the copper species, correlating with the surface area values in Table 1 because the value for TiO_2-0.5 decreases compared to TiO_2-0.2.

Fig. 6 presents the porous size distribution (PSD) of the powder catalyst samples. The TiO_2 sample (Fig. 6a) presented a bimodal PSD with a small fraction of micropores (<2 nm in diameter). The bimodal PSD showed one distribution of pore diameters ranging between 2.1 to 2.8 nm and a second distribution ranging between 2.8 and 100 nm, with maximum values at 2.3 and 4.3 nm, respectively. Both distributions ranged from mesoporous (2–50 nm) through macroporous (>50 nm) materials, with the greatest fraction of pore size diameters in the mesoporous range. The TiO_2-0.05 sample (Fig. 6b) presented a slight modification in its bimodal PSD compared to the TiO_2 sample, with maximum values at 3.5 and 5.3 nm and an increase in pore volume. The TiO_2-0.2 sample (Fig. 6c) showed a monomodal PSD with a pore size range between 2 and nearly 11 nm and a mode and maximum of 6 nm, thus remaining within the mesoporous range. The 0.2 wt% copper produced the most homogeneous PSD sample and the highest total pore volume of all the samples. The TiO_2-0.5 sample (Fig. 6d) showed a PSD very similar to the TiO_2-0.05 sample but with lower total pore volume. The 0.5 wt% copper decreased the capacity of percolation and permeability of the titania substrate. In summary, different quantities of copper added during synthesis caused textural changes in the TiO_2 catalysts; the properties are presented in Table 1. TiO_2-0.2 presented the most convenient textural and surface properties for a heterogeneous reaction.

3.5. XPS analysis

Fig. 7 shows the XPS results from Ti2p and O1s binding energy for TiO_2 and TiO_2-0.5. For all samples the C1s was taken as reference (284.94 eV). In Ti2p XPS spectra was found 3 peaks attributed to Ti^{2+}, Ti^{3+} and Ti^{4+} at 454.67, 457.07 and 458.74 eV in TiO_2 (Fig. 7a) and 455.09, 457.37 and 459.07 eV for TiO_2-0.5 (Fig. 7b). The satellite characteristic of TiO_2 was observed at 471.62 and 471.90 eV. Ti^{3+} was the majority specie obtained, due XPS is a surface analysis and the anatase phase is characterized by posses Ti^{3+} on the surface [42]. The O1s spectra present three peaks that appear in both samples (Fig. 7c,d), which are attributed to lattice oxygen from TiO_2 and copper oxides, surfaces hydroxyl oxygen/OH groups and adsorbed H_2O at 530.07, 531.05, 532.35 eV and 530.45, 531.31, 532.24 eV for TiO_2 and TiO_2-0.5, respectively [43–47]. The results shows that the TiO_2-0.5 sample present more adsorbed oxygen than TiO_2 with relative areas of 22.52% (surface OH groups) and 24.57% (adsorbed H_2O) compared with 19.79% and 19.85% from no doping sample. The above due doping Cu^{2+}ions into TiO_2 induce more oxygen vacancies, which cause the increase of adsorbed O_2 at the TiO_2 surface (hydroxyl groups) [43,48]. Oxygen vacancies have the advantages to increase the hydrophilic behavior and the water molecules prefer to occupy these oxygen vacancies to produce OH groups, which tend to make the surface hydrophilic [49,50].

The peaks at 932.88 and 952.63 eV in Fig. 8 are attributed to Cu^+ from Cu_2O and two at 934.05 and 953.19 to Cu^{2+} from CuO [44,51–53]. The satellites at 940.93 and 953.19 eV confirm the presence of Cu^{2+} [53,54]. It has been reported that Cu^+ could be generated during the XPS analysis [55]. Due the catalyst preparation (heat treatment with air) the presence of Cu^0 is not expected.
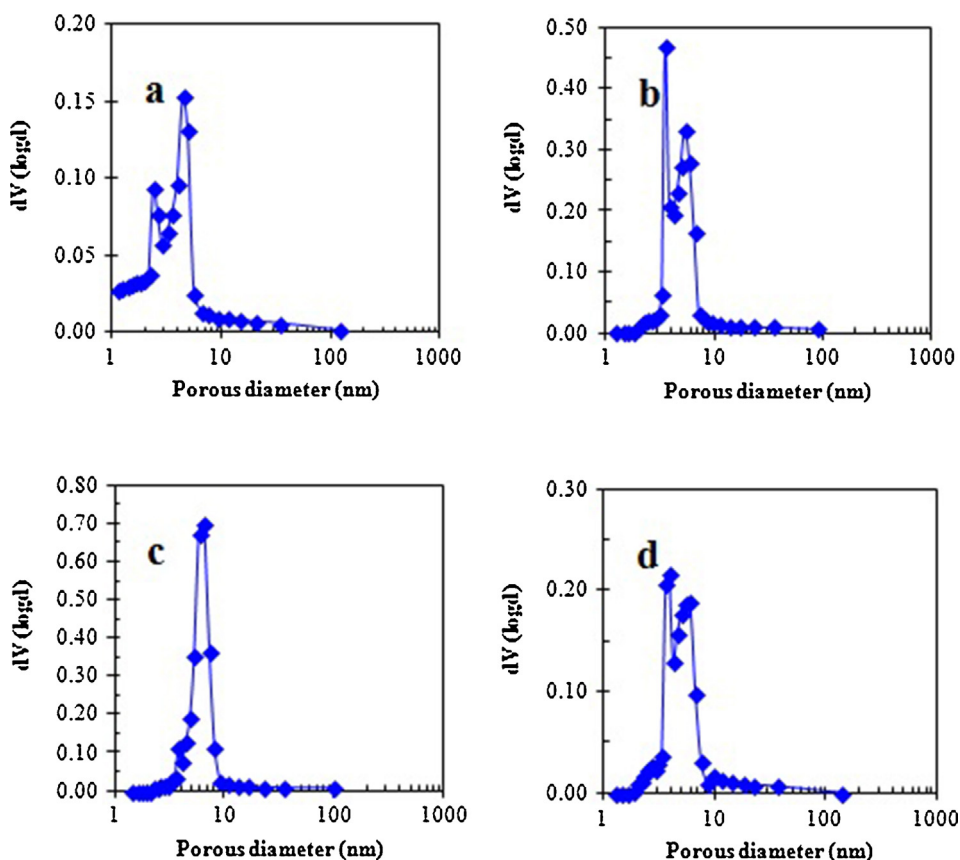
Fig. 6. PSD for samples TiO_2 (a), TiO_2-0.05 (b), TiO_2-0.2 (c), and TiO_2-0.5 (d).

The double peaks at 932.7 and 952.7 eV are attributed to Cu2p3/2 and Cu2p1/2 in $CuTiO_3(CuO·TiO_2)$ [56]. Relative low binding energy value for Cu2p XPS spectra and relative high binding energy value occur due to interactions between CuO and TiO_2 [57], for Ti2p should be ascribed to that the electrons of TiO_2 transfer to CuO since the Fermi level of CuO is lower than that of TiO_2 [56].

3.6. SEM images of powders

Fig. 9 compares the SEM micrographs of TiO_2 (Fig. 9a) and TiO_2-0.2 (Fig. 9b). The TiO_2 sample consisted of a compact surface in a solid piece formed from agglomerated particles of ~50 nm in diameter. The sample with 0.2 wt% copper also had ~50 nm particles but agglomerated into smaller and irregularly shaped pieces. The anatase TiO_2 crystalline phase was preserved with the addition of copper. The SEM images and textural analysis both show significant changes in the morphology of the photocatalysts, which is expected to be a positive influence on the degradation of TCE during photocatalytic reaction tests.

3.7. UV–vis Spectroscopy

Fig. 10 shows the UV–visible absorption spectra of photocatalyst powder samples.

The band gap energies (E_g) of the powder samples were calculated from the equation $\alpha(h\nu) = A(h\nu - E_g)^{m/2}$, where α is the absorption coefficient, $h\nu$ is the photon energy and $m = 1$ represents a direct transition between bands (valence band and conduction band). From the UV–vis spectra, E_g was calculated by extrapolating a straight line from the absorption curve to the abscissa; when α is zero, then $E_g = h\nu$.

Values of E_g for the samples are reported in Table 1. The band gap energies of the TiO_2 samples doped with copper ≥ 0.2 wt% are lower than the TiO_2 sample, associated with increased activity due to TiO_2/CuO interactions because Cu^{2+} traps electrons in the conduction band of TiO_2 and prevents charge recombination of the electrons and holes, favoring the formation of •OH [58]. Doping with transition metals such as Cu promotes charge separation and decreases the electron and hole recombination rate, thereby increasing the quantum yield of the photocatalytic process, thus favoring photocatalytic activity [59]. The optimum amount (%) of dopant for photocatalysis depends on the dopant species and its application. Adding a percentage larger than the optimum will have the opposite effect [60]. The TiO_2-0.2 and TiO_2-0.5 samples could be more competitive in the TCE photocatalytic tests.

The subsequent sections describe the analysis of the photocatalytic materials as deposited and washcoated into quartz tubes for use in the continuous annular reactor. Characterizing the powders can be very helpful, and their behavior is similar to the behavior of the same formulations that were deposited as photocatalytic washcoat into quartz tubes.

3.8. SEM images of photocatalytic-coated quartz tubes

The catalyst adheres to the substrate through electrostatic attraction after immersion of the quartz piece in sol. The isoelectric points of TiO_2 and quartz (SiO_2) are 6.2 and 1.8–2.7, respectively. At pH 4, the charge density on the surface of the titania is positive, while the quartz is negative [61].

It is necessary to provide an adequate structure to support the photocatalytic material. This structure can play an important role in the photocatalytic process because it can be inert or may be capable of interacting with the photocatalyst to improve or
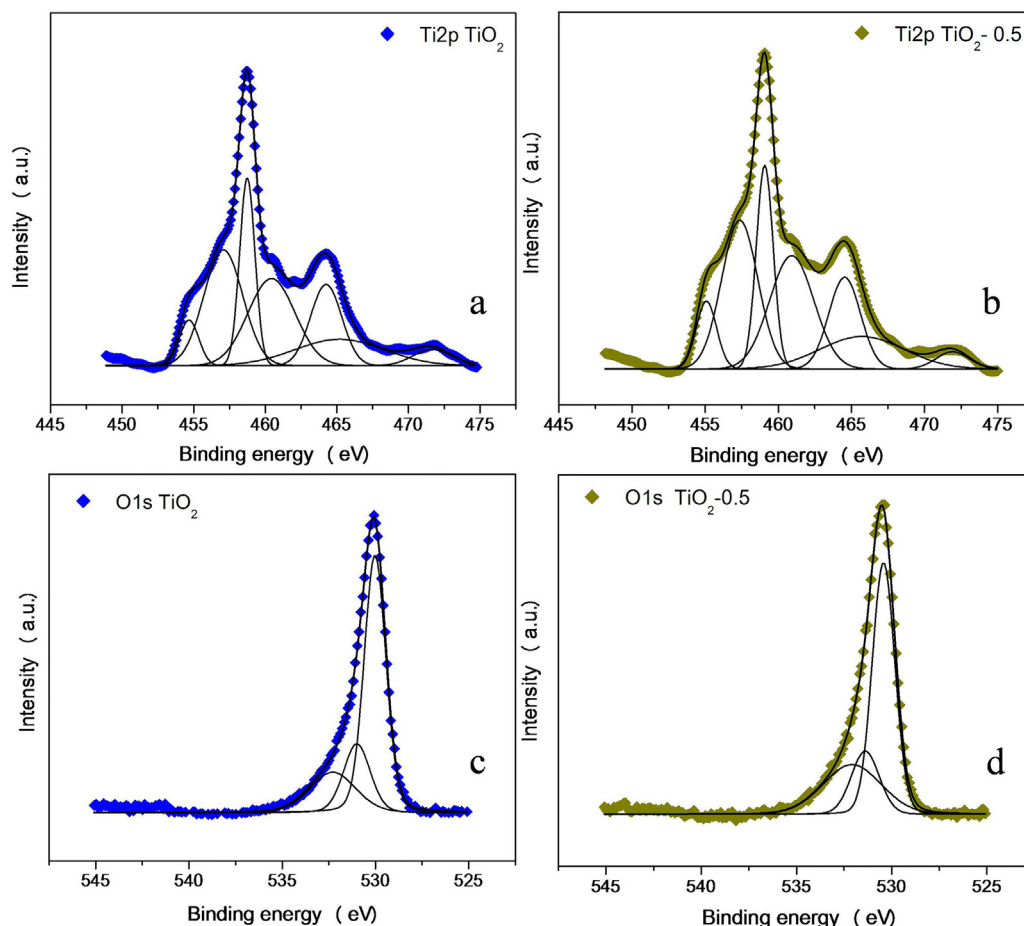
Fig. 7. High resolution XPS spectras Ti2p and O1s of TiO$_2$ (a, c) and TiO$_2$-0.5 (b, d).

decrease catalytic performance. Fig. 11 shows images of layers of TiO$_2$ and TiO$_2$-0.2 deposited on quartz material. The TiO$_2$ material supported on quartz shows agglomeration of particles in the range of 24–60 nm. The compaction and agglomeration of the particles is very similar to that observed in the powder sample (Fig. 9a). A shiny line forms the border between the quartz and the deposited material. The exterior face that will be in contact with UV radiation and TCE flow is very compact. Even following repeated deposition of sol during dip-coating, the TiO$_2$ did not show evidence of layers on the quartz structure support, only a layer of 36 nm on the external face, which showed better compaction than the underlying material. The total thickness of the deposited TiO$_2$ material was 385 nm. The TiO$_2$-0.2 sample showed a greater thickness of 554 nm (Fig. 9b). However, two layers can be identified in the image, and the surface is not planar, similar to the SEM powder images (Fig. 9b). The photo-catalytic supporting material was calcined at the same temperature as the powder samples (500 °C); therefore, the morphology is very similar for both applications.

3.9. Determination of thickness by ellipsometry

The index of refraction (an optical property) and film thickness can be determined by ellipsometry using plane-wave illumination at different angles of incidence ϕ with two orthogonal orientations of linear polarization. The ellipsometric parameters Ψ and Δ are defined as follows:

$$\tan \Psi e^{i\triangle} = \frac{Rp}{R_s}, \tag{1}$$

where R_p and R_s are the complex-amplitude reflectance coefficients in p-polarization (electric field vector in the plane of incidence) and s-polarization (electric field vector perpendicular to the plane of incidence), respectively [62,63]. A three-layer model is used to retrieve refractive index data and thickness measurements from the ellipsometric parameters Ψ and Δ [64]. Fig. 12 shows the results for fitting of the TiO$_2$ sample to the above equation with an incidence angle of 65°. The retrieved index of refraction was 2.9 ± 0.2 for TiO$_2$ materials, and the thickness was of 330 ± 41 nm, which was near the value measured by SEM. The measurements for other samples produced similar results.
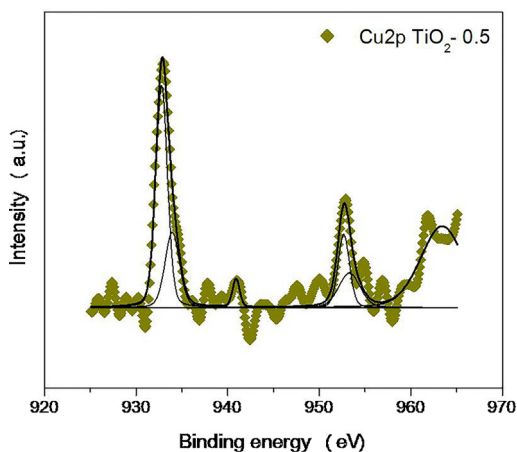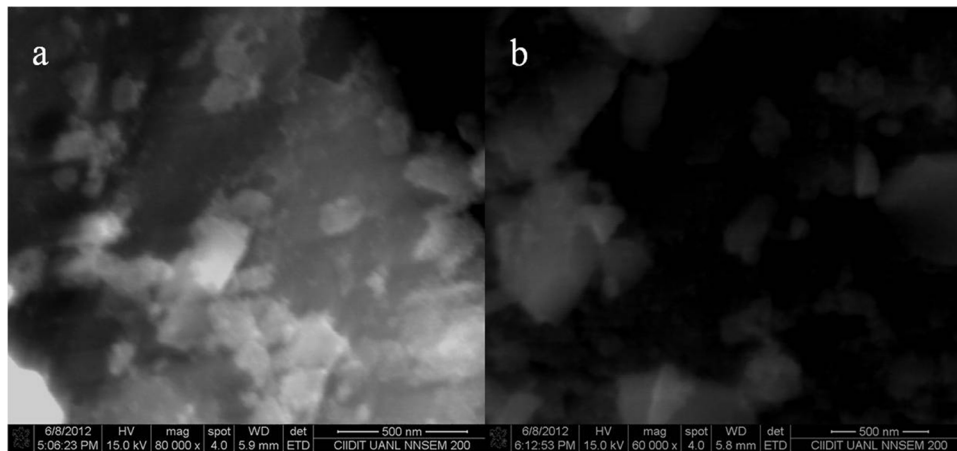

Fig. 8. High resolution XPS spectra Cu2p of TiO$_2$-0.5.

Fig. 9. SEM micrographs of TiO$_2$ (a) and TiO$_2$-0.2 samples.

3.10. Mass transfer evaluation in a tubular reactor

During photocatalytic degradation, mass transfer effect can play a significant role. A three-resistance model that considers mass transfer coefficients in modeling diffusion and reaction in catalytic materials is more useful and fundamental than the classical effectiveness-factor concept [37,39]. The external and internal mass transfer rates and the intrinsic kinetic reaction rate can be considered to be series resistances [58], as described in equation 2:

$$\frac{1}{k_{obs}} = \frac{1}{k_{rea}} + \frac{1}{k_{int}} + \frac{1}{k_{ext}}, \tag{2}$$

where k_{obs}, k_{rea}, k_{int} and k_{ext} are related to the observed degradation rate, the intrinsic kinetic reaction rate and the internal and external mass transfer rates, respectively.

Photocatalysis primarily implies surface reaction sites. It therefore seems coherent that internal diffusion by either the Knudsen or molecular mechanism is negligible [63]. The effect of external resistance must be considered only in the apparent degradation rate. Fig. 13 shows the mass-transfer effect in a continuous annular reactor.

The following mass balance equations can be written for a continuous stationary state [65]:

Fluid phase

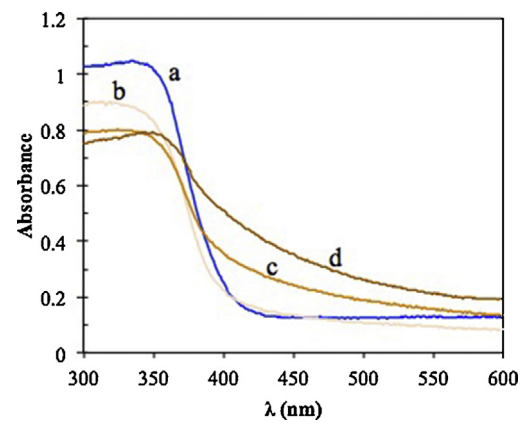$$u\frac{dC_A}{dz} + k_{ave-ext}a_v(C_{Ab} - C_{As}) = 0 \tag{3}$$

Fig. 10. UV–vis spectra of TiO$_2$ (a), TiO$_2$-0.05 (b), TiO$_2$-0.2 (c), and TiO$_2$-0.5 (d) powder samples calcined at 500 °C.

Solid phase

$$k_{ave-ext}a_v(C_{Ab} - C_{As}) = -r_A \tag{4}$$

where k_{av-ext} is the average mass coefficient (external), estimated using the following correlation [64]:

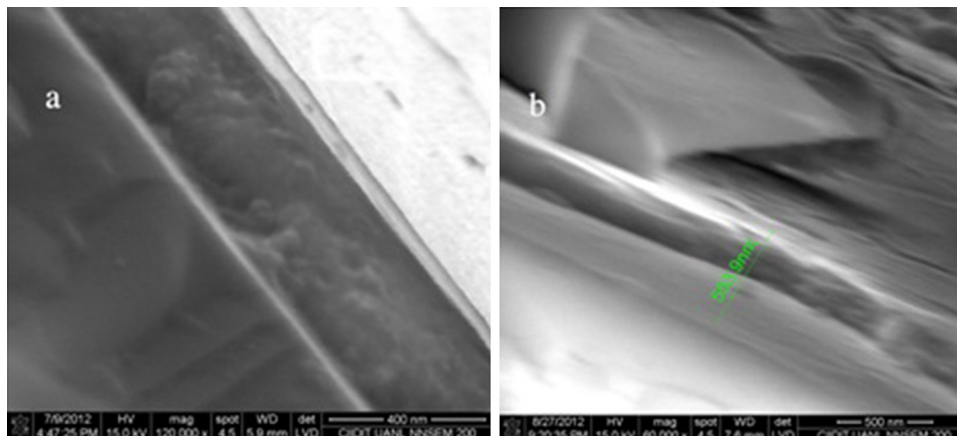$$Sh_{av} - 1.56Sc^{\frac{1}{3}}\left(\frac{Re\varphi d_g}{L}\right)^{0.34} X \geq 42 \times 10^{-4} \tag{5}$$

Fig. 11. SEM micrographs of washcoat of TiO$_2$ (a) and TiO$_2$-0.5 (b) samples.
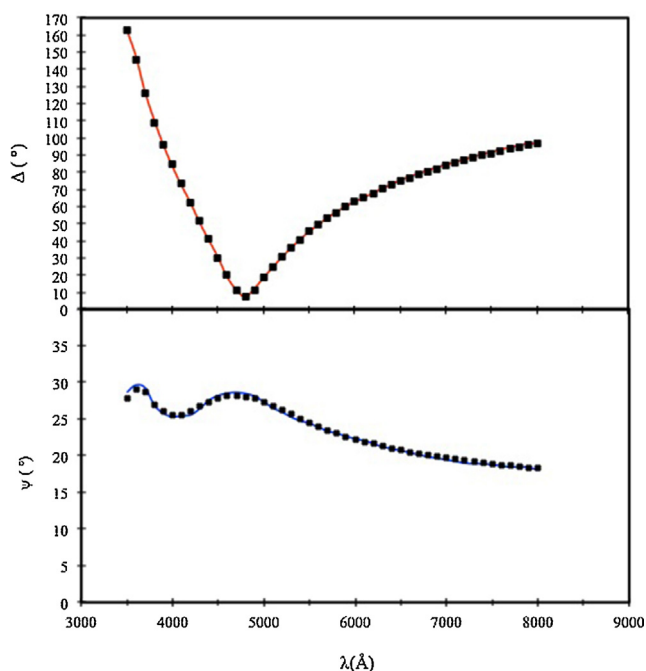
Fig. 12. Ellipsometric parameters Ψ and Δ as functions of the wave longitude at an incidence angle of 65°. The continuous line represents the Cauchy model fitting.

With

$$\varphi = \frac{\left[\frac{(1-a)}{a}\right]\left[\frac{1}{2} - \left(\frac{a^2}{(1-a^2)}\right)\ln\left(\frac{1}{a}\right)\right]}{\left[\left(\frac{(1+a^2)}{(1-a^2)}\right)\ln\left(\frac{1}{a}\right) - 1\right]} \tag{6}$$

The bulk concentration of species A (C_{Ab}) can be estimated in the next expression [66].

$$C_{Ab} = \frac{C_{Ain} - C_{Aout}}{2} \tag{7}$$

Eq. (7) can be expressed $\Delta C = C_{Ab} - C_{As}$ and solved from Eq. (4) [66]:

$$\triangle C_A = \frac{-r_A}{k_m a_v} \tag{8}$$

where $-r_A$ is the reaction rate in an isothermal differential reactor model and can easily be calculated because integrating the plug-flow equation is trivial, resulting in an average reaction rate value: $-r_{Aave}$ (a reasonable approximation at low conversion values) [66].

$$-r_A \text{ ave} \cong \frac{F_{Ao}(x_A)}{V} \tag{9}$$

The effect of mass transfer is significant if

$$\frac{\Delta C_A}{C_{Ab}} \geq 0.15 \tag{10}$$

Fig. 14 shows the mass transfer effect during degradation of TCE using the TiO$_2$-0.5 catalyst in a continuous annular reactor. The mass transfer effect is low at 70 °C and 500 ppm TCE at the
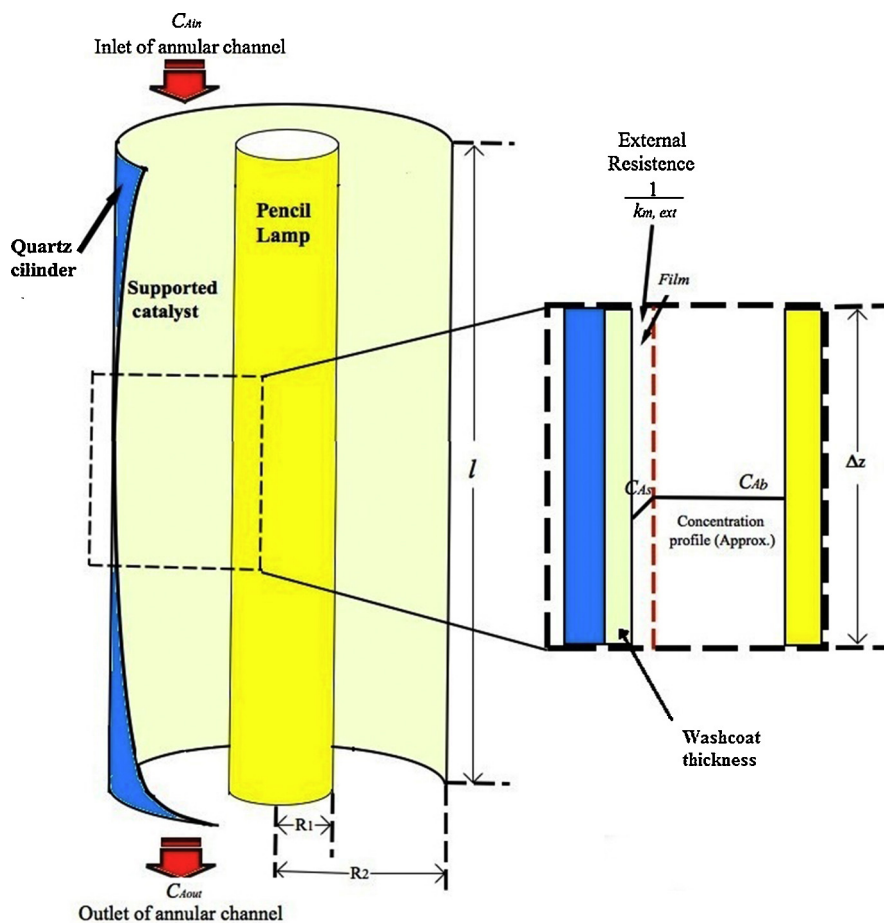

Fig. 13. Schematic diagram of the control volume that illustrates the fluid mass transfer during photocatalytic reaction on the washcoat (catalyst deposited by sol-gel method) with one external effective resistance approach in the continuous annular reactor.
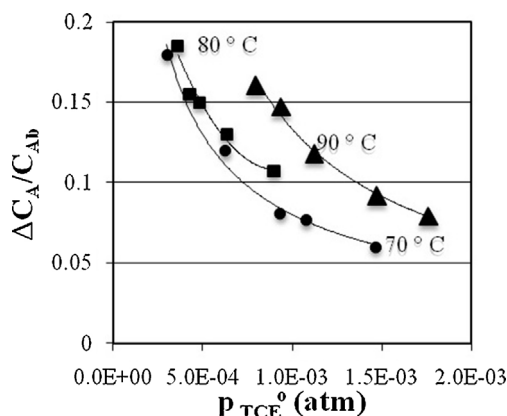
Fig. 14. Mass transfer effect of photocatalytic degradation of TCE on TiO$_2$-0.5 catalyst on continuous annular reactor at 60 ml/min.

inlet of the reactor. As the temperature increases, the mass transfer effect becomes more significant. The conversion values of TCE were always low; thus, it is important to use Eq. (9). For the other catalysts, similar results were obtained. The experimental reaction rate data obtained under these reaction conditions are viable for fitting to a model to determine the mechanisms of the surface reaction Fig. 15.

3.11. Kinetic data and model fitting

Fig. 15 shows the experimental surface reaction data for TCE degradation as a function of the partial inlet pressure of TCE in a photocatalytic continuous annular reactor at three temperatures using the four types of catalysts deposited on the interior wall surfaces of cylinders. The TiO$_2$-0.2 catalyst presented the highest values of TCE degradation. To correlate this finding, the TiO$_2$-0.2 catalyst presented TGA and DTA profiles where the physical and chemical desorption of the substance during calcination occurred at lower temperatures than the other catalyst formulations. This phenomenon caused particulate morphological surface differences. The Ti—O—Ti antisymmetric stretch of oxo-bridged titanium (IV) compounds on the surface showed the lowest vibration energy, which makes this compound more capable of interacting with external water or TCE molecules. Additionally, the TiO$_2$-0.2 catalyst showed a reduction in the mean crystallite size, as observed in DRX diffractograms, which produced the different morphologies evident in the SEM images and can be interpreted from the porosity characteristics. Although this catalyst had the most homogeneous PSD with the highest total pore volume, the photocatalytic reaction is carried out mainly on the surface; thus, larger surface areas definitely assist the capacity of percolation and permeability of the fluid phase. The most important characteristic that correlated to the high activity of the TiO$_2$-0.2 catalyst was its lower E_g values, favoring the production of •OH.

Eq. (11) shows a Langmuir–Hinshelwood (LH) surface kinetic model that considers two continuous active sites on the catalyst surface: one for actively adsorbing TCE species and the other for actively adsorbing H$_2$O [1,3]. Experimental kinetic data were fitted using the Microcal^{TM} Origin$^®$, version 6.0 software package, to estimate the parameters. The nonlinear least-squares fitting routine based on the Levenberg–Marquardt algorithm was employed.

$$r_{TCE} = kl^{\alpha} \left(\frac{K_1 P_{TCE}}{1 + K_1 P_{TCE} + K_2 P_{H_2O}} \right) \left(\frac{K_4 P_{H_2O}}{1 + K_3 P_{TCE} + K_4 P_{H_2O}} \right) \quad (11)$$

The LH model fit the doped catalysts better than the TiO$_2$ catalyst, possibly due to the assumption in the model of two different catalytically active sites that could be caused by copper doping.
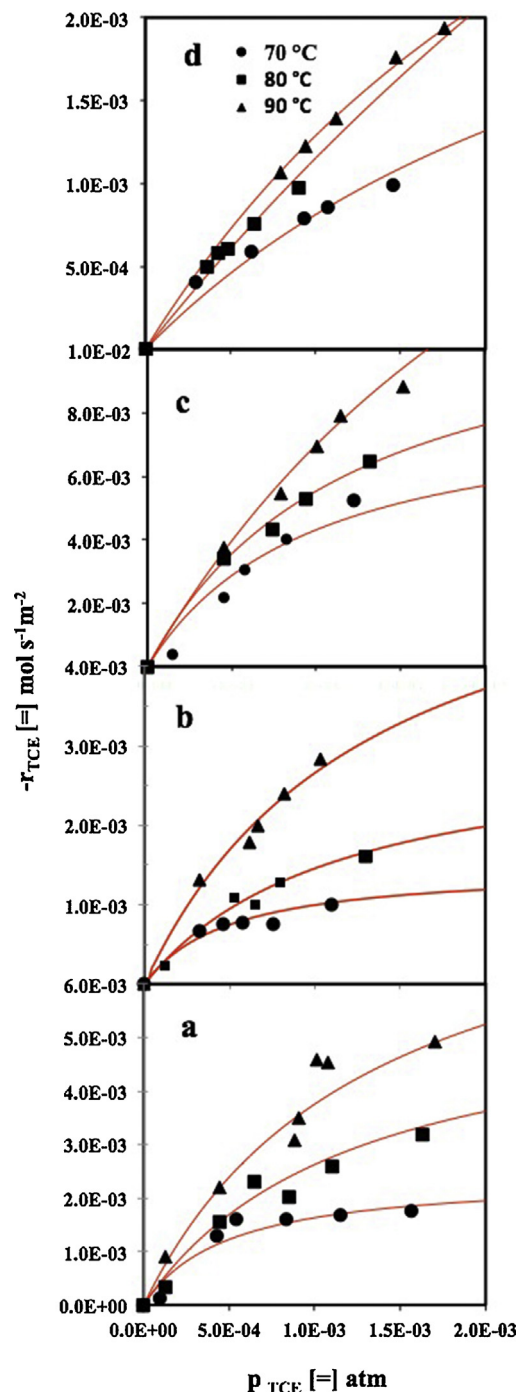

Fig. 15. Surface reaction rate data for photocatalytic degradation of trichloroethylene at three different temperatures on TiO$_2$ (a), TiO$_2$-0.05 (b), TiO$_2$-0.2 (c), and TiO$_2$-0.5 (d) catalysts. The continuous lines depict the fitting of the model equation (7).

Although this model has been used to study TCE photocatalytic degradation on pure TiO$_2$ photocatalyst [67] using a plate reactor, the mass transfer effect was not evaluated.

The estimated kinetic and adsorption equilibrium parameters can be used in the Arrhenius (Eq. (12)) and van't Hoff equation (Eq. (13)).

$$\ln k = \ln k^o - \frac{E_a}{RT} \quad (12)$$

$$\ln K = -\frac{\Delta H^o_{ads}}{RT} + \frac{\Delta S^o_{ads}}{T} \quad (13)$$

Table 2

Kinetic parameters and thermodynamic properties of constant of adsorption of model of Eq. (11) for the different catalysts tested in TCE degradation in photocalytic continuous annular reactor.

Sample	k^0 mol/s-m^2cat	k Ea (J/mol)	K_1 ΔH^o_{ads} (J/mol)	K_1 ΔS^o_{ads} (J/mol-K)	K_2 ΔH^o_{ads} (J/mol)	K_2 ΔS^o_{ads} (J/mol-K)	K_3 ΔH^o_{ads} (J/mol)	K_3 ΔS^o_{ads} (J/mol-K)	K_4 ΔH^o_{ads} (J/mol)	K_4 ΔS^o_{ads} (J/mol-K)
TiO_2	4.34×10^{19}	123.943	−50.944	−134	−35.008	−96	−51.099	−88	−58.358	−159
TiO_2-0.05	2.68×10^{20}	130.612	−51.810	−134	−34.974	−96	−51.292	−88	−56.856	−155
TiO_2-0.2	5.39×10^{12}	81.416	−43.367	−100	−58.890	−134	−59.605	−117	−43.141	−109
TiO_2-0.5	1.40×10^{26}	167.682	−102.784	−276	−111.336	−289	−47.275	−88	−64.308	−192

In the Arrhenius equation, k is the reaction rate constant, k^0 is the pre-exponential factor and E_a is the activation energy. In the van't Hoff expression, K is the adsorption equilibrium constant, and ΔH_{ads} and ΔS^o_{ads} are the standard enthalpy and entropy of adsorption, respectively.

In this work, the kinetic and adsorption constants for the LH model were obtained at three different temperatures. The Arrhenius and vanít Hoff equations were then fitted to these constants to determine k^0, E_a, ΔH^o_{ads} and ΔS^o_{ads}.

Table 2 compiles the activation energies and thermodynamic properties of the different catalysts calculated from the LH model.

Table 2 Kinetic parameters and thermodynamic properties of constant of adsorption of model of Eq. (11) for the different catalysts tested in TCE degradation in photocatalytic continuous annular reactor.

The kinetic and thermodynamic properties of catalysts TiO_2 and TiO_2-0.02 are very similar. The model was fitted to estimate the same grade of surface reaction rate; however, agreement with experimental data was better for the doped catalyst.

The activation energies of the surface reaction rate constants were high, while the equations require a low activation energy criterion (less than 10 kcal/mol $\approx$ 41.84 kJ/mol), indicative that the transport phenomenon is more dominant than an entirely reactive mechanism [68]. In this case, all values were higher than 41.84 kJ/mol. The TCE and H_2O molecules, adsorbed in neighboring active sites on a surface, then the H_2O is oxidezed by the holes (h^+) to produce OH. The reaction of TCE with •OH is extremely fast, making it the dominant step of the mechanism [3]. TiO_2-0.2 catalyst presented the lowest activation energy, supporting the finding that it had the best activity of the four catalysts. Doucet et al. [69] reported an E_a of 15,000 J/mol for photocatalytic TCE on TiO_2 (Degussa P25) in an annular reactor from 2 to 40 °C [69], using an LH model of one adsorption constant. In this work, the lowest activation energy was 81,416 J/mol at temperatures from 70 to 90 °C. Therefore, the mechanisms for surface reactions are different at higher temperatures.

When the van't Hoff equation was used to determine the adsorption equilibrium constants, the heats of adsorption for all samples and both models were negative (exothermic). Vannice et al. [70] recommended a set of criteria to validate the thermodynamic parameters extracted from kinetic fittings. First, adsorption is invariably exothermic; therefore, the enthalpy of adsorption is negative, i.e., $\Delta H^o_{ads} > 0$ ($Q_{ads} > 0$). Second, the entropy must decrease after adsorption, including the dissociative adsorption of a diatomic molecule. Therefore, $\Delta S^o_{ads} = S^o_{ads} - S^o_g < 0$, where S^o_g is the standard total entropy in the gas phase, which is 324.8 J/(mol · K) for trichloroethylene [70]. Third, a molecule or atom cannot lose more entropy than it possesses prior to adsorption; thus, $|\Delta S^o_{ads}| < S^o_g$. The thermodynamic values reported in Table 2 satisfy all of these criteria. The adsorption enthalpy of TCE at the first active site (K_1 constant) was the lowest for the TiO_2-0.2 catalyst and almost three times higher for the TiO_2-0.5 catalyst. Copper content >0.2 wt% attracts TCE to active site 1 more strongly; values are similar for the enthalpy of adsorption on active site 2. The TiO_2-0.5 catalyst showed the highest enthalpy of adsorption values for H_2O (K_2 and

K_4) for both types of sites. The adsorption of H_2O is strong on both types of sites for a copper content of 0.5 wt%, reasonably explained by the XPS results. For TiO_2-0.2 catalyst, TCE presented the best mobility at site 1 because $|\Delta S^o_{ads}|$ was the lowest, and H_2O presented the best mobility at site 2. In the range of copper studied, 0.2 wt% was optimal. CuO must be well dispersed within the photocatalyst to promote activity; otherwise, the formation of clusters by a high content (TiO_2-0.5 catalyst) causes recombination to take place and decreases activity. The water molecules strongly bonded to the catalysts can block the strong bond at the active sites [59]. Tests for durability and recyclability of the catalysts were not made but the catalyst was continuously used for 12 hours without the activity drop.

4. Conclusions

A Green Chemistry proposal was presented at the molecular level with the degradation of TCE, which was studied in moistened air using TiO_2 catalysts synthesized by sol–gel with different Cu doping: 0, 0.05, 0.2 and 0.5 wt% Cu in a continuous annular photocatalytic reactor. The 0.2 wt% Cu sample showed the most significant characteristics and photocatalytic activity: its crystallite size was the smallest, it showed the lowest vibrational energy for the Ti—O—Ti antisymmetric stretching of oxo-bridged titanium(IV) compounds on its surface, and it showed the most convenient microporosity characteristics. The characterization results of the powders were correlated with photocatalytic activity, and the sol–gel materials deposited on the interior walls of quartz cylinders showed similar morphologies. The most important feature of the catalyst doped with 0.2 wt% Cu was its lower E_g; its uniform porosity was also important and specific to this catalyst compared to the other three. To understand the behavior of the molecules on the surfaces, data were fitted to an LH model that considers two active sites: one for active TCE molecules and the other for active H_2O molecules. The activation energy and adsorption thermodynamic property constants proved that 0.2 wt% Cu content favored the mobility of both molecules, while 0.5 wt% Cu strongly blocked the active sites of bonded water.

References

[1] K.-H. Wang, H.-H. Tsai, Y.-H. Hsieh, Appl. Catal. B: Environ. 17 (1998) 313–320.
[2] V. Puddu, H. Choi, D.D. Dionysiou, G.L. Puma, Appl. Catal. B: Environ. 94 (2010) 211–218.
[3] G. Li Puma, I. Salvadó-Estivill, T.N. Obee, S.O. Hay, Sep. Purif. Technol. 67 (2009) 226–232.
[4] S. Yamazaki-Nishida, S. Cervera-March, K.J. Nagano, M.A. Anderson, K. Hori, J. Phys. Chem. 99 (1995) 15814–15821.
[5] V.H. Vu, J. Belkouch, A. Ould-Dris, B. Taouk, J. Hazard. Mater. 169 (2009) 758–765.
[6] T.H. Lim, S.D. Kim, Chemosphere 54 (2004) 305–312.
[7] J.B. Manley, P.T. Anastas, B.W. Cue Jr., J. Clean. Prod. 16 (2008) 743–750.

[8] S.K. Agarwal, J.J. Spivey, J.B. Butt, Appl. Catal. A: Gen. 82 (1992) 259–275.
[9] J.E. Atwater, J.R. Akse, J.A. McKinnis, J.O. Thompson, Appl. Catal. B: Environ. 11 (1996) L11–L18.
[10] J.R. González-Velasco, A. Aranzabal, R. López-Fonseca, R. Ferret, J.A. González-Marcos, Appl. Catal. B: Environ. 24 (2000) 33–43.
[11] E. Finocchio, G. Sapienza, M. Baldi, G. Busca, Appl. Catal. B: Environ. 51 (2004) 143–148.
[12] M.H. Kim, K.-H. Choo, Catal. Commun. 8 (2007) 462–466.
[13] A. Musialik-Piotrowska, K. Syczewska, Catal. Today 73 (2002) 333–342.
[14] D. Teschner, R. Farra, L. Yao, R. Schlögl, H. Soerijanto, R. Schomäcker, T. Schmidt, L. Szentmiklósi, A.P. Amrute, C. Mondelli, J. Pérez-Ramírez, G. Novell-Leruth, N. López, J. Catal. 285 (2012) 273–284.
[15] T. Tanimura, A. Yoshida, S. Yamazaki, Appl. Catal. B: Environ. 61 (2005) 346–351.
[16] K. Demeestere, J. Dewulf, T. Ohno, P.H. Salgado, H. Van Langenhove, Appl. Catal. B: Environ. 61 (2005) 140–149.
[17] S. Rehman, R. Ullah, A.M. Butt, N.D. Gohar, J. Hazard. Mater. 170 (2009) 560–569.
[18] L. Dibble, G. Raupp, Catal. Lett. 4 (1990) 345–354.
[19] M.R. Nimlos, W.A. Jacoby, D.M. Blake, T.A. Milne, Environ. Sci. Technol. 27 (1993) 732–740.
[20] K. Demeestere, A.D. Visscher, J. Dewulf, M.V. Leeuwen, H.V. Langenhove, Appl. Catal. B: Environ. 54 (2004) 261–274.
[21] H.-H. Ou, S.-L. Lo, J. Mol. Catal. A: Chem. 275 (2007) 200–205.
[22] H. Nishikiori, M. Furukawa, T. Fujii, Appl. Catal. B: Environ. 102 (2011) 470–474.
[23] P.B. Amama, K. Itoh, M. Murabayashi, Appl. Catal. B: Environ. 37 (2002) 321–330.
[24] G. Colón, M. Maicu, M.C. Hidalgo, J.A. Navío, Appl. Catal. B: Environ. 67 (2006) 41–51.
[25] S. Sun, J. Bao, C. Gao, J. Ding, Rare Metals 30 (2011) 147–152.
[26] H. Irie, S. Miura, K. Kamiya, K. Hashimoto, Chem. Phys. Lett. 457 (2008) 202–205.
[27] H. Nishikiori, T. Sato, S. Kubota, N. Tanaka, Y. Shimizu, T. Fujii, Res. Chem. Intermed. 38 (2012) 595–613.
[28] J.M. Herrmann, Top Catal. 34 (2005) 49–65.
[29] C.G. Silva, J.L. Faria, J. Mol. Catal. A: Chem. 305 (2009) 147–154.
[30] S. Vives, C. Meunier, Ceram. Int. 34 (2008) 37–44.
[31] M. Shui, Y. Song, Q. Wang, Y. Ren, Curr. Appl. Phys. 10 (2010) 1360–1365.
[32] Y.C. Zhu, C.X. Ding, Nanostruct. Mater. 11 (1999) 427–431.
[33] J. Baneshi, M. Haghighi, N. Jodeiri, M. Abdollahifar, H. Ajamein, Energy Convers. Manage. 87 (2014) 928–937.
[34] J.A. Chang, M. Vithal, I.C. Baek, S.I. Seok, J. Solid State Chem. 182 (2009) 749–756.
[35] R. Bensaha, H. Bensouyad, Synthesis, Characterization and Properties of Zirconium Oxide (ZrO2)-Doped Titanium Oxide (TiO$_2$) Thin Films Obtained via Sol–Gel Process 2012.
[36] H. Nishikiori, M. Hayashibe, T. Fujii, Catalysts 3 (2013) 363–377.
[37] E. Alizadeh-Gheshlaghi, B. Shaabani, A. Khodayari, Y. Azizian-Kalandaragh, R. Rahimi, Powder Technol. 217 (2012) 330–339.
[38] Y. Xie, X. Liu, A. Huang, C. Ding, P.K. Chu, Biomaterials 26 (2005) 6129–6135.
[39] C. Hammond, The basics of crystallography and diffraction, 1998.
[40] K. Sowri Babu, A. Ramachandra Reddy, C. Sujatha, K. Venugopal Reddy, A.N. Mallika, J. Adv. Ceram. 2 (2013) 260–265.
[41] K.S.W. Sing, D.H. Everett, R.A.W. Haul, L. Moscou, R.A. Pierotti, J. Rouquerol, T. Siemieniewsaka, Pure Appl. Chem. 57 (1985) 603–619.
[42] M.Y. Kang, H.J. Yun, S. Yu, W. Kim, N.D. Kim, J. Yi, J. Mol. Catal. A: Chem. 368–369 (2013) 72–77.
[43] S. Wang, K.K. Meng, L. Zhao, Q. Jiang, J.S. Lian, Ceram. Int. 40 (2014) 5107–5110.
[44] Y. Xu, J.-a. Li, L.-f. Yao, L.-h. Li, P. Yang, N. Huang, Surf. Coat. Technol. 261 (2015) 436–441.
[45] B. Erdem, R.A. Hunsicker, G.W. Simmons, E.D. Sudol, V.L. Dimonie, M.S. El-Aasser, Langmuir 17 (2001) 2664–2669.
[46] Z. Rui, Y. Huang, Y. Zheng, H. Ji, X. Yu, J. Mol. Catal. A: Chem. 372 (2013) 128–136.
[47] S.S. Lee, H. Bai, Z. Liu, D.D. Sun, Appl. Catal. B: Environ. 140–141 (2013) 68–81.
[48] T. Watanabe, A. Nakajima, R. Wang, M. Minabe, S. Koizumi, A. Fujishima, K. Hashimoto, Thin Solid Films 351 (1999) 260–263.
[49] R. Wang, N. Sakai, A. Fujishima, T. Watanabe, K. Hashimoto, J. Phys. Chem. B 103 (1999) 2188–2194.
[50] M. Nakamura, S. Kato, T. Aoki, L. Sirghi, Y. Hatanaka, J. Appl. Phys. 90 (2001) 3391–3395.
[51] E. Vigil, F.A. Fernández-Lima, J.A. Ayllón, E. Pedrero, I. Zumeta, B. González, L. Curbelo, H.D. Fonseca Filho, M.E.H. Maia da Costa, C. Domingo, M. Behar, F.C. Zawislak, Micropor. Mesopor. Mater. 109 (2008) 560–566.
[52] I.H. Tseng, J.C.S. Wu, H.-Y. Chou, J. Catal. 221 (2004) 432–440.
[53] C. Sun, J. Zhu, Y. Lv, L. Qi, B. Liu, F. Gao, K. Sun, L. Dong, Y. Chen, Appl. Catal. B: Environ. 103 (2011) 206–220.
[54] L. Huang, F. Peng, F.S. Ohuchi, Surf. Sci. 603 (2009) 2825–2834.
[55] S. Xu, A.J. Du, J. Liu, J. Ng, D.D. Sun, Int. J. Hydrogen Energy 36 (2011) 6560–6568.
[56] Q. Wu, J. Li, W. Zhang, H. Qian, W. She, H. Pan, J. Wen, X. Zhang, X. Liu, X. Jiang, J. Mater. Chem. B 2 (2014) 6738–6748.
[57] R. Yang, L. Yang, T. Tao, F. Ma, M. Xu, Z. Zhang, Appl. Surf. Sci. 288 (2014) 363–368.
[58] A.L. Linsebigler, G. Lu, J.T. Yates, Chem. Rev. 95 (1995) 735–758.
[59] G. Li, N.M. Dimitrijevic, L. Chen, T. Rajh, K.A. Gray, J. Phys. Chem. C 112 (2008) 19040–19044.
[60] R.M.A. Azzam, N.M. Bashara, D. Thorburn Burns, Anal. Chim. Acta 199 (1987) 283–284.
[61] J. Yu, J. Xiong, B. Cheng, S. Liu, Appl. Catal. B: Environ. 60 (2005) 211–221.
[62] G. Harland, E.A. Tompkins. Irene Handbook of Ellipsometry 1, 6–13, 2005.
[63] W. Rzodkiewicz, A. Panas, J. Phys.: Conf. Ser. 181 (12035) (2009) 1–7.
[64] M.R. Saleem, P. Silfsten, S. Honkanen, J. Turunen, Thin Solid Films 520 (2012) 5442–5446.
[65] W.E.S. Byron, R. Bird, N. Edwin, Lightfoot, (English) 2nd Edition 912 (2010).
[66] C.J. Lucio-Ortiz, J.R. De la Rosa, A. Hernández-Ramírez, E.M. López-Cuellar, G. Beltrán-Pérez, R. del Carmen Miranda Guardiola, C.D. Pedroza-Solís, Coll. Surf. A: Physicochem. Eng. Aspects 371 (2010) 81–90.
[67] R.E. Treybal, MassTransfer Oper. 3 (1980) 45–78.
[68] M.A. Vannice, S.H. Hyun, B. Kalpakci, W.C. Liauh, J. Catal. 56 (1979) 358–362.
[69] N. Doucet, F. Bocquillon, O. Zahraa, M. Bouchy, Chemosphere 65 (2006) 1188–1196.
[70] D.R. Lide, Handbook Chemistry and Physics, 2, 58, 1975.